Check for updates

Constructing Ultra-Shallow Near-Edge States for Efficient and Stable Perovskite Solar Cells

Xueliang Zhu, Wenqi Xiong, Chong Hu, Kangwei Mo, Man Yang, Yanyan Li, Ruiming Li, Chen Shen, Yong Liu, Xiaoze Liu, Sheng Wang, Qianqian Lin, Shengjun Yuan, Zhengyou Liu, and Zhiping Wang*

Electronic band structure engineering of metal-halide perovskites (MHP) lies at the core of fundamental materials research and photovoltaic applications. However, reconfiguring the band structures in MHP for optimized electronic properties remains challenging. This article reports a generic strategy for constructing near-edge states to improve carrier properties, leading to enhanced device performances. The near-edge states are designed around the valence band edge using theoretical prediction and constructed through tailored material engineering. These states are experimentally revealed with activation energies of around 23 milli-electron volts by temperature-dependent time-resolved spectroscopy. Such small activation energies enable prolonged carrier lifetime with efficient carrier transition dynamics and low non-radiative recombination losses, as corroborated by the millisecond lifetimes of microwave conductivity. By constructing near-edge states in positive-intrinsic-negative inverted cells, a champion efficiency of 25.4% (25.0% certified) for a 0.07-cm^2 cell and 23.6% (22.7% certified) for a 1-cm^2 cell is achieved. The most stable encapsulated cell retains 90% of its initial efficiency after 1100 h of maximum power point tracking under one sun illumination (100 mW cm^{-2}) at 65 °C in ambient air.

1. Introduction

Metal-halide perovskites (MHP) have undergone magnificent advancements as low-cost and highly efficient solar energy harvesting materials for photovoltaic applications.[1–3] In less than a decade, the power conversion efficiency (PCE) has surged to 26.1% for a single-junction perovskite solar cell (PSC),[4] approaching 80% of the Shockley–Queisser limits. This remarkable progress is a result of intensive efforts on composition,

interface, and defect engineering,[5–8] To fully unlock the potential of PSCs, it demands minimizing non-radiative recombination losses and increasing charge carrier density with an in-depth understanding of underlying physical mechanisms.[9] This demand can be addressed by sophisticated band structure engineering, which focuses on profound MHP materials science and aims for preferred electronic properties.

Band structure engineering, rooted in a comprehensive knowledge of detailed band structures, has become a major research direction for PSCs. Similar to conventional solar materials (e.g., crystalline silicon, gallium arsenide), various material strategies have been tried out to reconfigure valence/conduction bands for improved electronic properties by introducing dopants. For example, specific technical approaches, such as precursor engineering[10,11] and post-treatments,[12,13] B-site substitution,[14] impurity doping[15,16] and charge transfer doping,[17–19] are developed to tune the Fermi level within the band gap for increased carrier density. Even though some cases introduce additional electronic disorders in perovskites,[20–22] the corresponding device performances are apparently improved. However, efficient and reliable engineering for preferred electronic properties remains challenging, due to the lack of comprehensive investigation of MHP band structures and global engineering strategies.

Here, we start with a theoretical analysis of band structures and propose a generic strategy for constructing near-valence-band-edge states. This strategy is then realized through tailored material engineering and experimentally demonstrated to simultaneously improve carrier density and lifetime, and prevent MHP degradation. By testing the enhanced device performance, the underlying generic principle for this strategy is summarized and can be applied for more comprehensive band structure engineering.

2. Results and Discussion

It has been theoretically and experimentally demonstrated that lattice distortion or octahedral tilting only changes the size of the band gap while no new state shall be formed,[23,24] The
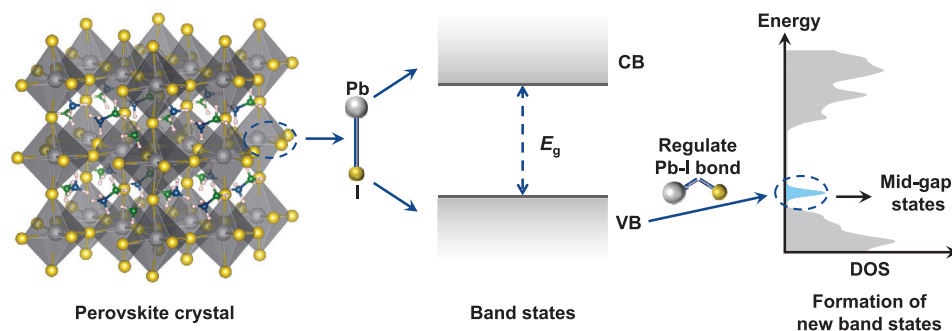
X. Zhu, W. Xiong, C. Hu, K. Mo, M. Yang, Y. Li, R. Li, C. Shen, Y. Liu, X. Liu, S. Wang, Q. Lin, S. Yuan, Z. Liu, Z. Wang
School of Physics and Technology, Hubei Luojia Laboratory, Key Lab of Artificial Micro- and Nano-Structures of Ministry of Education
School of Microelectronics Wuhan University
Wuhan 430072, China
E-mail: zp.wang@whu.edu.cn
X. Zhu, K. Mo, M. Yang, X. Liu, S. Wang, S. Yuan, Z. Wang
Wuhan Institute of Quantum Technology
Wuhan 430206, China

**ADVANCED
SCIENCE NEWS**

www.advancedsciencenews.com

**ADVANCED
MATERIALS**

www.advmat.de

Figure 1. Band structure engineering in metal-halide perovskite semiconductors.

reconfiguration of valence bands (VB) of lead-iodide perovskites is of great importance to manipulate electronic properties. The VB of lead-iodide perovskites is contributed by I-5p states and the conduction band (CB) is mainly derived from Pb-6p states,[23,25] as schematically described in **Figure 1**. By regulating the Pb—I bond, near-edge states could be formed with new VB configuration for distinct electronic behaviors. In the theoretical design, we focus on modifying the density of states (DOS) distribution of mixed-cation perovskites due to their high efficiency and stability in solar cells,[26,27] We introduce 3-fluoro-phenethylammonium iodide (F-PEAI) in the perovskite body and phenethylammonium iodide (PEAI) on the perovskite surface (Figure S1, Supporting Information). The PEAI and their derivatives have been extensively studied as effective defect passivation agents in perovskites,[28–30] Here we use the PEAI and F-PEAI molecules as the dopants to modify the band structure of perovskites. This strategy would allow us to investigate any potential improvements while retaining highly desirable features such as long carrier lifetimes.[31]

2.1. Density Function Theory Analysis

We first study the interaction between the PEAI/F-PEAI molecules and perovskites using density function theory (DFT) calculations. We focus on the $FA_{8/9}MA_{1/9}PbI_3$ perovskite with defects and construct two models: the control model which has MAI or FAI vacancy (V_{MAI} or V_{FAI}) in the surface and body, and target model, where the surface and body MAI/FAI vacancies are modified with PEAI and F-PEAI molecules, respectively. **Figure 2a,b** shows the DOS distribution of the control and target perovskites, respectively. The control sample exhibits similar results to the perfect perovskite, while new states near the valence band maximum appear in the target sample. These new states are found to have originated from the insertion of PEAI/F-PEAI molecules, which break one of the Pb—I bonds in the body and push one of the I ions near the vacancy away from the surface. Our results confirm that the surface dissociative I ions contribute to the near-edge states, while the internally broken I ions cause the localized states only within the VB (Figure S2, Supporting Information). To understand the origin of the broken Pb—I bonds, we calculate the bond energy for a perfect model and for a model with F-PEAI added to the body. Our calculations show that the introduction of F-PEAI gives rise to the formation of F—Pb bond and the break of the internal Pb—I bond, which significantly re-

duces the Pb—I bond energy at the surface from 1.81 to 0.29 eV (Figure 2c,d). Figure 2e,f further manifests that the F in the F-PEAI molecule tends to adsorb to the underlying Pb atoms, forming a stronger Pb—F ionic bond that replaces the original Pb—I bond (B6) due to the stronger electronegativity of F compared to I. At the same time, the bottom Pb atoms move down and the liberated I atoms rise, causing an obvious increase in the distance of the internal Pb—I bond (B6). The charge density difference indicates that the charge reconstruction of the internal Pb—I bonds (B5) is enhanced, and the internal I atoms gain more electrons. Compared with the B2, the shortened Pb—I bond (B1) represents a stronger bond strength. However, this enhancement of the internal Pb—I bond strength (B5) will reduce the electron transfer from Pb to I atoms in the surface Pb—I bond (B4). As a consequence, the surface Pb—I bond (B4) becomes longer, leading to less charge reconstruction and a significant decrease in its bond energy. This explains why the I ions are prone to dissociation at the surface. However, the introduction of F-PEAI in the body only weakens the surface Pb—I bond energy, and it is not sufficient to cause the dissociation of I ions at the surface, that is, cannot produce the near-edge states (Figure S3b, Supporting Information). After, the PEAI is introduced onto the surface, and it is easy to break the weakened Pb—I bond, causing the dissociation of I ions (Figure S2, Supporting Information). Thus, to create the near-edge states, it is necessary to simultaneously introduce F-PEAI into the body and PEAI onto the surface. A more specific explanation of both processes is summarized in Note S1, Supporting Information. We also calculate the total energy of the systems and find that the energy is lower for the system with dissociative I ions than for the system with unbroken Pb—I bonds (Figure S4, Supporting Information). This supports the rationale of the target model. Moreover, our DFT calculations suggest that introducing the near-edge states should elevate the Fermi level, leading to typical n-doping. This prediction is confirmed by the Kelvin probe measurements (Figure S5, Supporting Information).

To experimentally assess the proposed near-edge states, we conduct time-resolved photoluminescence (TRPL) and time-resolved microwave conductivity (TRMC) measurements[32,33] for control and target perovskite films. In the experimental setting, we focus on triple-cation lead iodide perovskites and incorporate F-PEAI in the precursor solution to mimic the body doping and apply a post-treatment on the as-crystallized perovskite films with PEAI to reproduce the surface doping in the theoretical design. More experimental details are depicted in the Supporting Information. All the TRPL spectra show single exponential
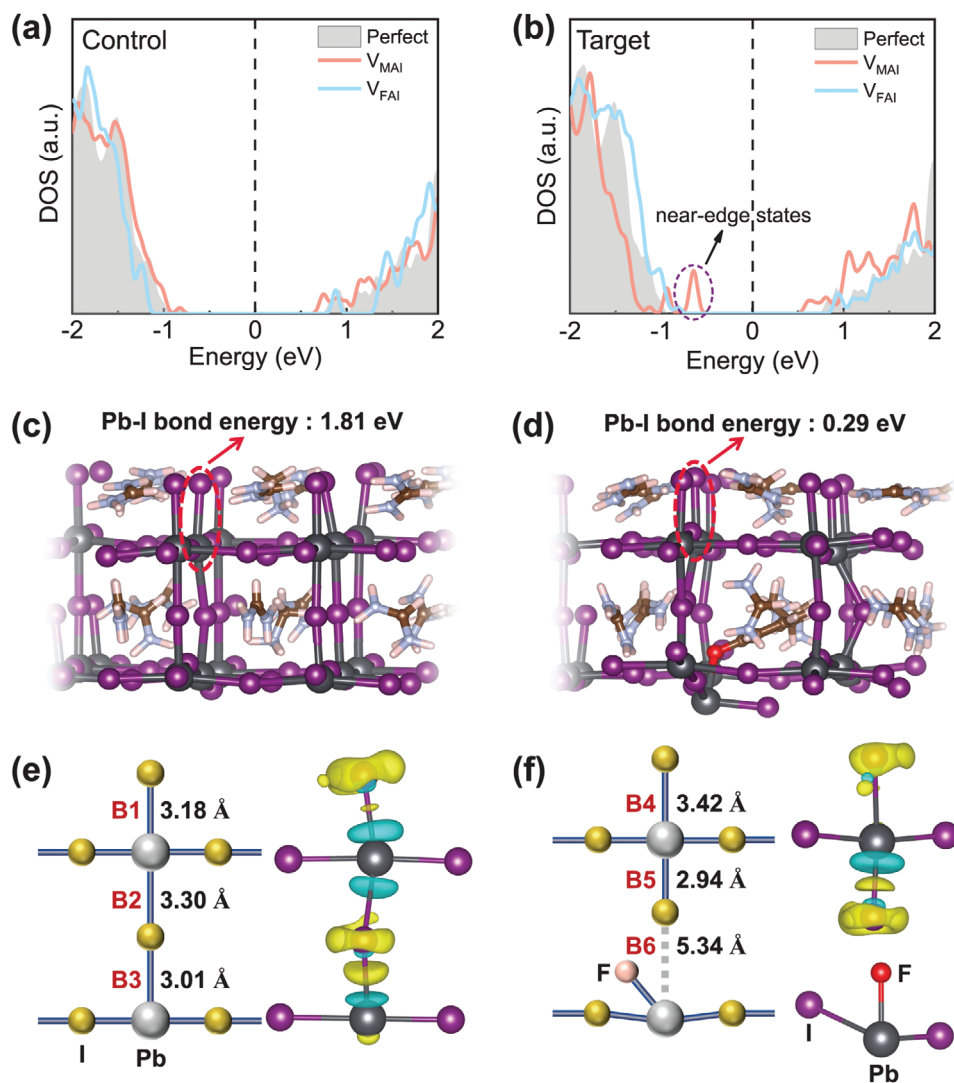
Figure 2. The DOS distribution of a) control and b) target samples. The DOS of perfect $FA_{8/9}MA_{1/9}PbI_3$ perovskite is represented by the shaded area. The orange and blue lines in DOS denote the modifications at the MAI and FAI locations, respectively. The calculated Pb—I bond energy for c) a perfect model and d) a model with F-PEAI added to the body. The corresponding theoretical model, bond distances and charge density differences for e) a perfect model and f) a model with F-PEAI added to the body. The yellow and blue electron clouds represent charge accumulation and depletion, respectively. Isosurface: 0.003 e bohr^{-3}.

decays at early time windows of 10 µs (**Figure 3**a), indicating the dominance of trap-assisted monomolecular recombination for the initial dynamics.[34,35] The fitted carrier lifetime for the initial dynamics increases dramatically from 2165 ns for the control sample to 5473 ns for the target sample, due to the reduced non-radiative recombination owing to defect passivation by the F-PEAI/PEAI molecules.[36,37] The TRMC decays suggest that the target sample effectively enhances the carrier mobility (Figure 3b,c). More importantly, both the TRPL and TRMC decay for the target sample display flat tails which are speculated to have originated from charge trapping and de-trapping process.[32,38] Combined with the DFT results, we thus propose the formation of shallow near-edge states where the carriers repeatedly trapped or released with negligible non-radiative recombination losses.

To gain in-depth understanding of the newly formed near-edge states, we perform temperature-dependent TRPL measurements on the control and target sample, as shown in Figure 3d,e. Clearly, the control sample shows less variations in decay lifetime (i.e., the inverse of monomolecular recombination rate, k_1) with different temperatures. In stark contrast, the target sample shows strong temperature dependence. With all fitted temperature-dependent monomolecular recombination rates for both samples, we are able to extract the activation energies (E_a) of the near-edge states as $\ln(k_1) \approx \exp(\frac{-E_a}{k_B T})$ where k_B is Boltzmann constant (Figure 3f). The E_a is fitted to be only ≈7 meV for the control sample, indicating the absence of near-edge states. By contrast, the E_a is 23 meV for the target sample, which is very close to the thermal energy at room temperature ($k_B T \approx 26$ meV@300 K). This evidence points to the existence of new states near the band edge

**ADVANCED
SCIENCE NEWS**

www.advancedsciencenews.com

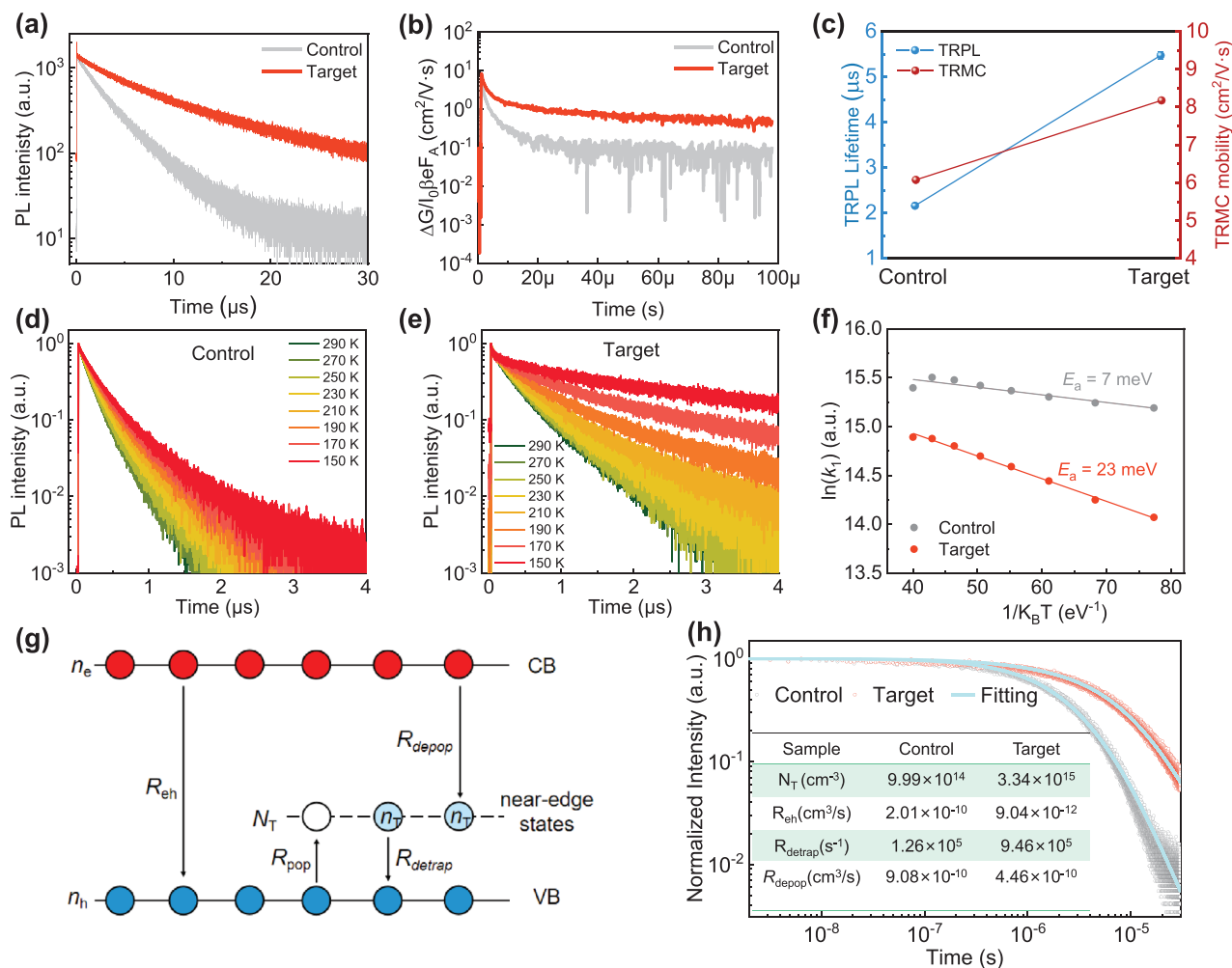**ADVANCED
MATERIALS**

www.advmat.de

Figure 3. a) TRPL decays of the control and target perovskite films deposited on glass substrates. b) Photoconductivity transients of perovskite films measured by TRMC. c) Plots of the extracted TRPL lifetimes and TRMC mobilities. Temperature-dependent TRPL spectra of the d) control and e) target perovskite films deposited on glass substrates. f) Determination of the active energies of the near-edge states by the Arrhenius equation. g) Schematic illustration of the charge-carrier recombination model in the presence of near-edge states. h) Analysis of trapping–de-trapping processes via TRPL fittings.

and the depth of the states is extremely shallow, corroborating our DFT calculation of the near-edge states in Figure 2b. These states provide a profound playground for the carrier dynamics with highly efficient trapping and de-trapping activities even at room temperature, which would be beneficial for device operation.

We thus build a dynamics model with carrier trapping and de-trapping model.[39,40] and look into the carrier processes in the control and target samples (Figure 3g). The model is simplified to be of three states, that is, the edges of CB and VB, and the near-edge states. The near-edge states are considered to be mainly hole traps with trapping and de-trapping activities because they are close to the VB edge. After photo-excitations, there are several decay channels for the excited electrons in CB and the excited holes in VB. Besides the bimolecular electron-hole recombination (radiative channel) with a rate constant of R_{eh}, the other decay channels all involve trap-mediated recombination near the band-edge of VB. These channels refer to the trapping popula-

tion process of capturing holes from the VB-edge with a rate constant of R_{pop}, the de-trapping process of releasing holes back to the VB-edge with a rate constant of R_{detrap}, and the depopulation process of nonradiative trapped hole recombination with a rate constant of R_{depop}. Based on the fitting of TRPL with the model, the R_{eh} is significantly slowed down by about 20 times for the target sample than the control sample (see the fitted parameters for all samples in the inset table in Figure 3h). The slow-down trend is consistent with the carrier lifetime based on the simplified single-exponential decay dynamics, but this slow-down ratio ($\approx$20) is much larger than the single-exponential lifetime ratio of 2.5. This is due to the totally different dynamics of trap-mediated recombination in the target sample. The trap density and de-trapping rate R_{detrap} both increase significantly for target sample, while the trapping population and depopulation rate constants (R_{pop} and R_{depop}) do not change much. In this way, the traps act as an additional carrier reservoir to exchange carriers with valence near-edge. This is further supported by the elevated Fermi
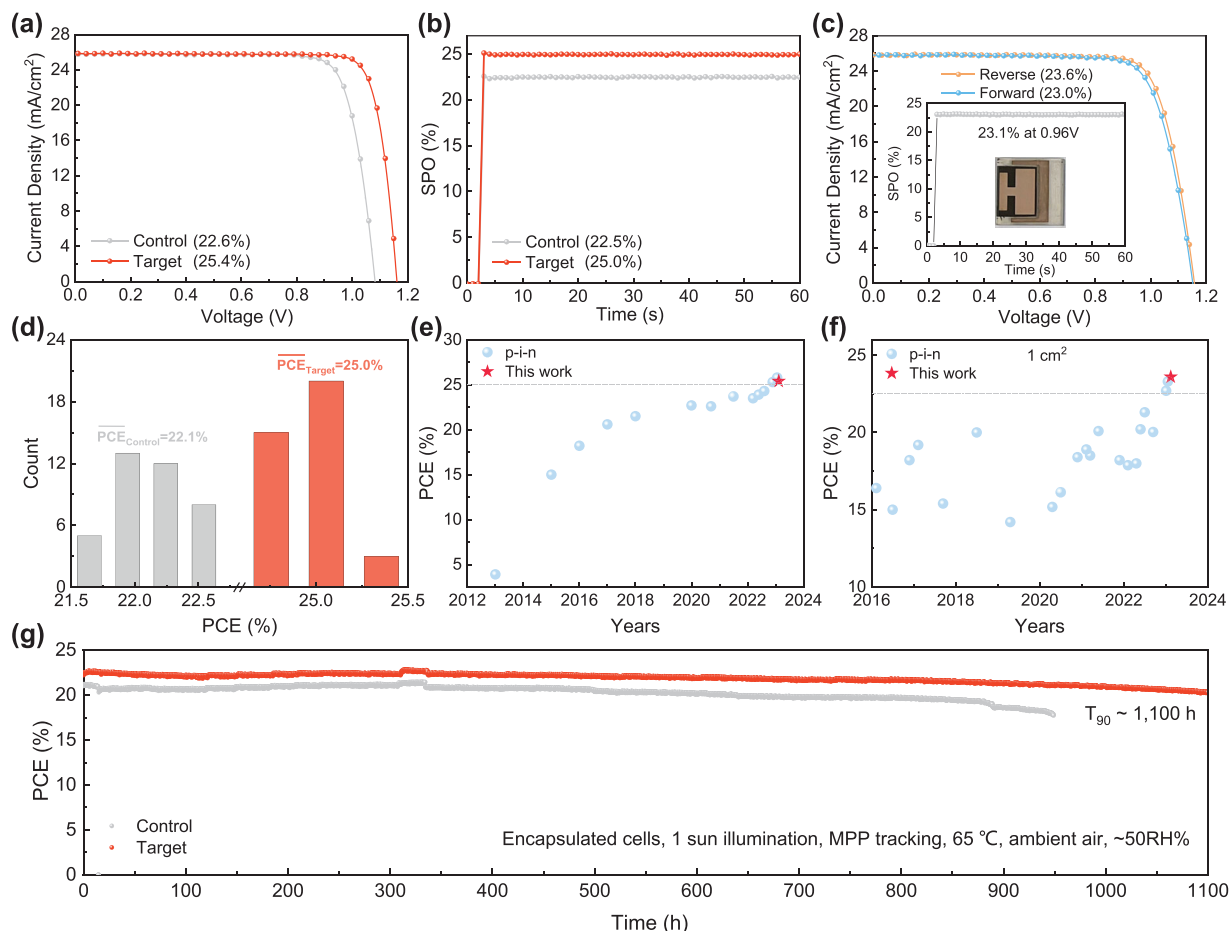
**ADVANCED
SCIENCE NEWS**

www.advancedsciencenews.com

**ADVANCED
MATERIALS**

www.advmat.de

Figure 4. a) J–V characteristics of the optimized devices measured from forward bias to short circuit under simulated AM 1.5 G sunlight. b) The SPO of the champion cells is measured by holding the cell at a fixed voltage near maximum power point on the J–V curve for 60 s. c) J–V curves of 1-cm² PSCs (inset shows the SPO and the photograph of the device). d) A statistical distribution of the PCE was obtained from four batches of devices (40 cells per type). e) Reported champion certified or J–V scanned PCE for inverted PSCs compared to the PCE achieved in this work. f) Evolution of the reported high-profile efficiencies of 1-cm² inverted devices. g) Encapsulated solar cells over time. The cells are aged under one sun continuous illumination at 65 °C in ambient air with a relative humidity of around 50%.

levels (Figure S5, Supporting Information) and corroborated with our DFT calculation (Figure 2a,b). Detailed explanations regarding the model are given in Note S2, Supporting Information.

We now inspect the impact of near-edge states on solar cell performance. We fabricate positive-intrinsic-negative (p-i-n) inverted cells with a structure of FTO/NiO$_x$/Me-4PACz/FA$_{0.9}$MA$_{0.06}$Cs$_{0.04}$PbI$_3$/C$_{60}$/BCP/Cu. Based on systematically optimizing the device performance (Figure S6, Supporting Information), we finally choose the F-PEAI molecule for the body and the PEAI molecule for the surface. **Figure 4a** shows the current density–voltage (J–V) curves of the highest-performing cells, and full device characteristics and external quantum efficiency (EQE) are given in the Supporting Information (Figures S7–S9 and Table S1, Supporting Information). Clearly, the modification mainly affects the open-circuit voltage (V_{oc}) and fill factor (FF) (Figure 4b). The best target device delivers a scanned PCE of 25.4% and a steady-state power output (SPO) of 25.0%, amongst the highest value for NiO$_x$-based PSCs (Figure S10, Supporting Information). The V_{oc} reaches 1.16 V at a band gap of 1.52 eV (see Tauc plot of the perovskite

film and the derivative of the EQE spectrum in Figures S11 and S12, Supporting Information), corresponding to a low V_{oc} deficit of 360 mV. One of the best-performing target devices is certified by an independent solar cell accredited laboratory, achieving a certified PCE of 25.01% and an SPO of 24.44% (see certification reports in Figure S13, Supporting Information). We also fabricate 1-cm² large-area cells and the target devices show a champion PCE of 23.6% in Figure 4c and certified 22.7% (see the EQE and certification reports in Figures S14 and S15, Supporting Information). Figure 4d exhibits an excellent reproducibility, with an average PCE of 22.1% for the control device and 25.0% for the target device. We further compare our results with the champion small- and large-area inverted PSCs reported over the past 10 years (Figure 4e,f and Table S2, Supporting Information). The efficiency attained in this work is almost identical to the current state-of-the-art.

Another important point to ascertain is whether the beneficial impact derived from the near-edge states will endure throughout extended periods of operation. We carry out maximum power point (MPP) tracking of the target cells under one

sun illumination (100 mW cm^{-2}, see the spectrum of the light source in Figure S16, Supporting Information) at an elevated temperature of 65 °C in ambient air with a relative humidity of around 50%, corresponding to international summit on organic photovoltaic stability (ISOS-L-3) aging standard.[41] We first age non-encapsulated devices for 120 h (Figure S17, Supporting Information), and find that the control device loses nearly 20% efficiency after aging. In stark contrast, the target device is relatively stable, losing only 10% of its initial PCE after 120 h. We further perform long-term MPP tracking on encapsulated devices. The time to 90% of the decay (T$_{90}$) is 1100 h for the target device, which is higher than the 950 h for the control device (Figure 4g and Figure S18, Supporting Information). Double-injection (DI) current measurement suggests that the ion migration is largely suppressed in the target devices (Figure S19 and Note S3, Supporting Information). This can be further supported by the theoretical calculation where the target samples show higher binding energy with defects than the control samples (Figure S20, Supporting Information). Figure S21, Supporting Information demonstrates that the presence of F ion in the perovskite bulk stabilizes the local structure via strengthened bonding with Pb, which is in good agreement with the previous report.[42] Experimentally, we conduct Raman spectroscopy measurements and observe a low-frequency Raman band at 230 cm^{-1} (Figure S22a, Supporting Information), corresponding to the vibration of the Pb—F bond.[43] X-ray photoelectron spectroscopy spectra (Figure S22b, Supporting Information) reveal that, in contrast to the control sample, the Pb 4f peaks shift to lower binding energies for the target sample. This further indicates the decrease of under-coordinated Pb^{2+} due to the strong interaction between Pb and F.[44,45]

3. Conclusion

In conclusion, multiple key factors are responsible for the enhanced device performance. First, the growth defects are passivated by F-PEAI/PEAI, reducing non-radiative recombination and extending carrier lifetimes. Second, the ultra-shallow near-edge states generated in the target samples effectively elongate electron-hole recombination through efficient trap and de-trapping processes. This results in reduced non-radiative recombination losses, increased carrier densities within finite time windows, and ultimately over 25% efficiencies in the target devices. Third, the reinforced binding energies between the F-PEAI/PEAI molecules and the defects mitigate ion migrations, enabling stable power output over long-term operation at an elevated temperature. Our work not only demonstrates an effective method for achieving high-performance devices, but also underscores the importance of understanding the impacts of foreign molecules on electronic states in perovskites.

Supporting Information

Supporting Information is available from the Wiley Online Library or from the author.

Acknowledgements

Conflict of Interest

The authors declare no conflict of interest.

Data Availability Statement

The data that support the findings of this study are available from the corresponding author upon reasonable request.

Keywords

[1] Q. Jiang, J. Tong, Y. Xian, R. A. Kerner, S. P. Dunfield, C. Xiao, R. A. Scheidt, D. Kuciauskas, X. Wang, M. P. Hautzinger, R. Tirawat, M. C. Beard, D. P. Fenning, J. J. Berry, B. W. Larson, Y. Yan, K. Zhu, *Nature* **2022**, *611*, 278.

[2] M. J. Jeong, K. M. Yeom, S. J. Kim, E. H. Jung, J. H. Noh, *Energy Environ. Sci.* **2021**, *14*, 2419.

[3] M. Kim, J. Jeong, H. Lu, T. K. Lee, F. T. Eickemeyer, Y. Liu, I. W. Choi, S. J. Choi, Y. Jo, H.-B. Kim, S. Mo, Y.-K. Kim, H. Lee, N. G. An, S. Cho, W. R. Tress, S. M. Zakeeruddin, A. Hagfeldt, J. Y. Kim, M. Grätzel, D. S. Kim, *Science* **2022**, *375*, 302.

[4] NREL efficiency chart, http://www.nrel.gov/ncpv/images/efficiency_charg.jpg.

[5] Z. Wang, Q. Lin, F. P. Chmiel, N. Sakai, L. M. Herz, H. J. Snaith, *Nat. Energy* **2017**, *2*, 17135.

[6] J. Kang, L.-W. Wang, *J. Phys. Chem. Lett.* **2017**, *8*, 489.

[7] D. Luo, W. Yang, Z. Wang, A. Sadhanala, Q. Hu, R. Su, R. Shivanna, G. F. Trindade, J. F. Watts, Z. Xu, T. Liu, K. Chen, F. Ye, P. Wu, L. Zhao, J. Wu, Y. Tu, Y. Zhang, X. Yang, W. Zhang, R. H. Friend, Q. Gong, H. J. Snaith, R. Zhu, *Science* **2018**, *360*, 1442.

[8] Y. Hou, X. Du, S. Scheiner, D. P. McMeekin, Z. Wang, N. Li, M. S. Killian, H. Chen, M. Richter, I. Levchuk, N. Schrenker, E. Spiecker, T. Stubhan, N. A. Luechinger, A. Hirsch, P. Schmuki, H. P. Steinrück, R. H. Fink, M. Halik, H. J. Snaith, C. J. Brabec, *Science* **2017**, *358*, 1192.

[9] Z. Wang, Q. Lin, B. Wenger, M. G. Christoforo, Y. Lin, M. T. Klug, M. B. Johnston, L. M. Herz, H. J. Snaith, *Nat. Energy* **2018**, *3*, 855.

[10] Q. Wang, Y. Shao, H. Xie, L. Lyu, X. Liu, Y. Gao, J. Huang, *Appl. Phys. Lett.* **2014**, *105*, 163508.

[11] G. Paul, S. Chatterjee, H. Bhunia, A. J. Pal, *J. Phys. Chem. C* **2018**, *122*, 20194.

[12] D. Song, P. Cui, T. Wang, D. Wei, M. Li, F. Cao, X. Yue, P. Fu, Y. Li, Y. He, B. Jiang, M. Trevor, *J. Phys. Chem. C* **2015**, *119*, 22812.

[13] A. Zohar, I. Levine, S. Gupta, O. Davidson, D. Azulay, O. Millo, I. Balberg, G. Hodes, D. Cahen, *ACS Energy Lett.* **2017**, *2*, 2408.

[14] Y. Chen, H. Jing, F. Ling, W. Kang, T. Zhou, X. Liu, W. Zeng, Y. Zhang, L. Qi, L. Fang, M. Zhou, *Chem. Phys. Lett.* **2019**, *722*, 90.

**ADVANCED
SCIENCE NEWS**

www.advancedsciencenews.com

**ADVANCED
MATERIALS**

www.advmat.de

[15] M. Abdi-Jalebi, M. I. Dar, A. Sadhanala, S. P. Senanayak, M. Franckevičius, N. Arora, Y. Hu, M. K. Nazeeruddin, S. M. Zakeeruddin, M. Grätzel, R. H. Friend, *Adv. Energy Mater.* **2016**, *6*, 1502472.

[16] Y. Yang, X. Zou, Y. Pei, X. Bai, W. Jin, D. Chen, *J. Mater. Sci.* **2018**, *29*, 205.

[17] S. Olthof, K. Meerholz, *Sci. Rep.* **2017**, *7*, 40267.

[18] E. E. Perry, J. G. Labram, N. R. Venkatesan, H. Nakayama, M. L. Chabinyc, *Adv. Electron. Mater.* **2018**, *4*, 1800087.

[19] H. Chen, Y. Zhan, G. Xu, W. Chen, S. Wang, M. Zhang, Y. Li, Y. Li, *Adv. Funct. Mater.* **2020**, *30*, 2001788.

[20] T. Shi, W. J. Yin, F. Hong, K. Zhu, Y. Yan, *Appl. Phys. Lett.* **2015**, *106*, 103902.

[21] Y. Yamada, M. Hoyano, R. Akashi, K. Oto, Y. Kanemitsu, *J. Phys. Chem. Lett.* **2017**, *8*, 5798.

[22] A. M. Ulatowski, A. D. Wright, B. Wenger, L. R. V. Buizza, S. G. Motti, H. J. Eggimann, K. J. Savill, J. Borchert, H. J. Snaith, M. B. Johnston, L. M. Herz, *J. Phys. Chem. Lett.* **2020**, *11*, 3681.

[23] M. R. Filip, G. E. Eperon, H. J. Snaith, F. Giustino, *Nat. Commun.* **2014**, *5*, 5757.

[24] D. Ghosh, A. Aziz, J. A. Dawson, A. B. Walker, M. S. Islam, *Chem. Mater.* **2019**, *31*, 4063.

[25] J. Zhu, S. Park, O. Y. Gong, C. H. Sohn, Z. Li, Z. Zhang, B. Jo, W. Kim, G. S. Han, D. H. Kim, T. K. Ahn, J. Lee, H. S. Jung, *Energy Environ. Sci.* **2021**, *14*, 4903.

[26] M. Saliba, T. Matsui, J.-Y. Seo, K. Domanski, J.-P. Correa-Baena, M. K. Nazeeruddin, S. M. Zakeeruddin, W. Tress, A. Abate, A. Hagfeldt, M. Grätzel, *Energy Environ. Sci.* **2016**, *9*, 1989.

[27] X. Zhu, C. F. J. Lau, K. Mo, S. Cheng, Y. Xu, R. Li, C. Wang, Q. Zheng, Y. Liu, T. Wang, Q. Lin, Z. Wang, *Nano Energy* **2022**, *103*, 107849.

[28] H. Chen, S. Teale, B. Chen, Y. Hou, L. Grater, T. Zhu, K. Bertens, S. M. Park, H. R. Atapattu, Y. Gao, M. Wei, A. K. Johnston, Q. Zhou, K. Xu, D. Yu, C. Han, T. Cui, E. H. Jung, C. Zhou, W. Zhou, A. H. Proppe, S. Hoogland, F. Laquai, T. Filleter, K. R. Graham, Z. Ning, E. H. Sargent, *Nat. Photonics* **2022**, *16*, 352.

[29] S. Yu, J. Meng, Q. Pan, Q. Zhao, T. Pullerits, Y. Yang, K. Zheng, Z. Liang, *Energy Environ. Sci.* **2022**, *15*, 3321.

[30] J. Tong, Q. Jiang, A. J. Ferguson, A. F. Palmstrom, X. Wang, J. Hao, S. P. Dunfield, A. E. Louks, S. P. Harvey, C. Li, H. Lu, R. M. France, S. A. Johnson, F. Zhang, M. Yang, J. F. Geisz, M. D. McGehee, M. C. Beard, Y. Yan, D. Kuciauskas, J. J. Berry, K. Zhu, *Nat. Energy* **2022**, *7*, 642.

[31] S. D. Stranks, S. D. Stranks, G. E. Eperon, G. Grancini, C. Menelaou, M. J. P. Alcocer, T. Leijtens, L. M. Herz, A. Petrozza, H. J. Snaith, *Science* **2014**, *342*, 341.

[32] F. Yao, Q. Lin, *ACS Photonics* **2022**, *9*, 3165.

[33] S. Bai, R. Li, H. Huang, Y. Qi, Y. Xu, J. Song, F. Yao, O. J. Sandberg, P. Meredith, A. Armin, Q. Lin, *Appl. Phys. Rev.* **2022**, *9*, 021405.

[34] Z. Chen, Z. Li, C. Zhang, X. F. Jiang, D. Chen, Q. Xue, M. Liu, S. Su, H. L. Yip, Y. Cao, *Adv. Mater.* **2018**, *30*, 1801370.

[35] A. A. B. Baloch, F. H. Alharbi, G. Grancini, M. I. Hossain, M. K. Nazeeruddin, N. Tabet, *J. Phys. Chem. C* **2018**, *122*, 26805.

[36] E. Akman, S. Akin, *Adv. Mater.* **2021**, *33*, 2006087.

[37] J. Wang, J. Zhang, Y. Zhou, H. Liu, Q. Xue, X. Li, C. C. Chueh, H. L. Yip, Z. Zhu, A. K. Y. Jen, *Nat. Commun.* **2020**, *11*, 177.

[38] H. Hempel, T. J. Savenije, M. Stolterfoht, J. Neu, M. Failla, V. C. Paingad, P. Kužel, E. J. Heilweil, J. A. Spies, M. Schleuning, J. Zhao, D. Friedrich, K. Schwarzburg, L. D. A. Siebbeles, P. Dörflinger, V. Dyakonov, R. Katoh, M. J. Hong, J. G. Labram, M. Monti, E. Butler-Caddle, J. Lloyd-Hughes, M. M. Taheri, J. B. Baxter, T. J. Magnanelli, S. Luo, J. M. Cardon, S. Ardo, T. Unold, *Adv. Energy Mater.* **2022**, *12*, 2102776.

[39] M. J. Trimpl, A. D. Wright, K. Schutt, L. R. V. Buizza, Z. Wang, M. B. Johnston, H. J. Snaith, P. Müller-Buschbaum, L. M. Herz, *Adv. Funct. Mater.* **2020**, *30*, 2004312.

[40] F. Lang, M. Jošt, J. Bundesmann, A. Denker, S. Albrecht, G. Landi, H. C. Neitzert, J. Rappich, N. H. Nickel, *Energy Environ. Sci.* **2019**, *12*, 1634.

[41] M. V. Khenkin, E. A. Katz, A. Abate, G. Bardizza, J. J. Berry, C. Brabec, F. Brunetti, V. Bulović, Q. Burlingame, A. Di Carlo, R. Cheacharoen, Y. B. Cheng, A. Colsmann, S. Cros, K. Domanski, M. Dusza, C. J. Fell, S. R. Forrest, Y. Galagan, D. Di Girolamo, M. Grätzel, A. Hagfeldt, E. von Hauff, H. Hoppe, J. Kettle, H. Köbler, M. S. Leite, S. (Frank) Liu, Y. L. Loo, J. M. Luther, et al., *Nat. Energy* **2020**, *5*, 35.

[42] N. Li, S. Tao, Y. Chen, X. Niu, C. K. Onwudinanti, C. Hu, Z. Qiu, Z. Xu, G. Zheng, L. Wang, Y. Zhang, L. Li, H. Liu, Y. Lun, J. Hong, X. Wang, Y. Liu, H. Xie, Y. Gao, Y. Bai, S. Yang, G. Brocks, Q. Chen, H. Zhou, *Nat. Energy* **2019**, *4*, 408.

[43] Z. Li, J. Park, H. Park, J. Lee, Y. Kang, T. K. Ahn, B. G. Kim, H. J. Park, *Nano Energy* **2020**, *78*, 105159.

[44] M. Li, H. Gao, L. Yu, S. Tang, Y. Peng, C. Zheng, L. Xu, Y. Tao, R. Chen, W. Huang, *Small* **2021**, *17*, 2102090.

[45] J. Yuan, X. Zhang, J. Sun, R. Patterson, H. Yao, D. Xue, Y. Wang, K. Ji, L. Hu, S. Huang, D. Chu, T. Wu, J. Hou, J. Yuan, *Adv. Funct. Mater.* **2021**, *31*, 2170196.